Research Article Vol. 10, No. 12 / December 2023 / Optica 1633

Dose-efficient *in vivo* X-ray phase contrast imaging at micrometer resolution by Bragg magnifiers

Rebecca Spiecker,[1,*] Pauline Pfeiffer,[2] Adyasha Biswal,[3,4] Mykola Shcherbinin,[1] Martin Spiecker,[5] Holger Hessdorfer,[3] Mathias Hurst,[3] Yaroslav Zharov,[1] Valerio Bellucci,[1,6] Tomáš Faragó,[3] Marcus Zuber,[3] Annette Herz,[7] Angelica Cecilia,[3] Mateusz Czyzycki,[1] Carlos Sato Baraldi Dias,[3] Dmitri Novikov,[8] Lars Krogmann,[2] Elias Hamann,[3] Thomas van de Kamp,[1,3] and Tilo Baumbach[1,3]

[1]Laboratory for Applications of Synchrotron Radiation (LAS), Karlsruhe Institute of Technology (KIT), Kaiserstr. 12, Karlsruhe, 76131, Germany
[2]Department of Entomology, State Museum of Natural History, Rosenstein 1, Stuttgart, 70191, Germany
[3]Institute for Photon Science and Synchrotron Radiation (IPS), Karlsruhe Institute of Technology (KIT), Hermann-von-Helmholtz-Platz 1, Eggenstein-Leopoldshafen, 76344, Germany
[4]Centre for Organismal Studies, Heidelberg University, Im Neuenheimer Feld 230, Heidelberg, 69120, Germany
[5]Physikalisches Institut, Karlsruhe Institute of Technology (KIT), Kaiserstr. 12, Karlsruhe, 76131, Germany
[6]European X-Ray Free-Electron Laser Facility GmbH, Holzkoppel 4, Schenefeld, 22869, Germany
[7]Julius Kühn-Institute, Institute for Biological Control, Schwabenheimer Str. 101, Dossenheim, 69221, Germany
[8]Deutsches Elektronen-Synchrotron DESY, Notkestr. 85, Hamburg, 22607, Germany
*rebecca.spiecker@kit.edu

Received 19 July 2023; revised 11 October 2023; accepted 15 October 2023; published 7 December 2023

X-ray imaging enables the study of morphodynamic and physiological processes in living organisms. However, the required photon flux increases with the desired spatial resolution and with it the requirements for dose efficiency. We realize full-field imaging at micrometer resolution close to the highest possible dose efficiency. This is achieved by combining propagation-based phase contrast with Bragg crystal optics and a high-Z single-photon-counting detector, all designed for X-ray energies that allow minimal dose for a given image quality. We prove the superior imaging performance compared to conventional systems and, in particular, show a substantial increase in dose efficiency for high spatial frequencies that comprise the relevant high-resolution components of the image. We demonstrate the potential of the technique by a behavioral *in vivo* study of submillimeter-sized parasitoid chalcid wasps within their host eggs before and during emergence. The findings show that the technique opens up new possibilities for dose-sensitive studies at micrometer resolution, not only in life sciences but also in materials research.

https://doi.org/10.1364/OPTICA.500978

1. INTRODUCTION

X-ray imaging is a powerful tool for non-destructive imaging of internal structures in optically opaque samples. High-resolution imaging enables visualization of the morphology of small organisms, addressing biological and biomedical questions in a broad range of fields [1–8], e.g., developmental biology [3,7] or functional morphology [2,5]. In this context, also time-resolved *in vivo* X-ray imaging has gained increasing interest [9–16]. However, the fact that biological samples tolerate only a limited radiation dose due to radiation damage is a major issue, especially in absorption-based X-ray imaging and particularly for *in vivo* studies. With increasing resolution, the X-ray flux density has to be increased, which further exacerbates the dose issue.

Significant efforts have been made to reduce the dose. The most prominent approach is phase contrast imaging, revealing phase changes of the X-rays penetrating through the specimen. For light elements and thus in weakly absorbing soft tissues, phase variation dominates absorption by several orders of magnitude [17]. Appropriate methods are propagation-based phase contrast (PB-PCI) [18–20] and differential phase contrast (DPCI) imaging techniques [21–23]. While DPCI techniques are mainly used in the medium resolution range of several to several hundred micrometers [23,24], PB-PCI is usually the method of choice for micrometer and sub-micrometer resolution. PB-PCI exploits the coherent self-interference of the transmitted wavefield behind the sample, which increasingly evolves into intensity contrast as the propagation distance increases. The object information is extracted from the recorded intensity patterns by suitable reconstruction algorithms [19,20,25]. Taking advantage of the high flux density and brilliance of modern synchrotron sources, high frame rates at micrometer resolution have become feasible. However, only very short time sequences of a few seconds to minutes could be realized so far, limited by severe radiation damage of the biological specimens [10–15]. In these *in vivo* studies, conventional

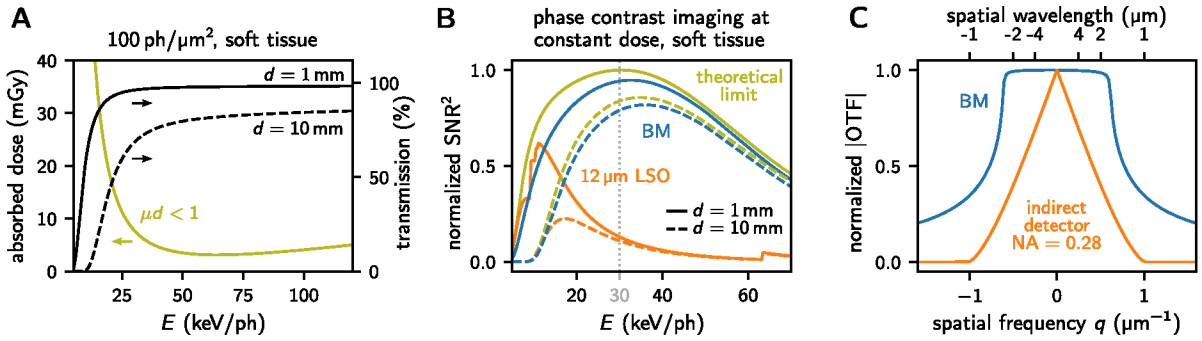

Fig. 1. Considerations for dose-efficient X-ray imaging. (A) Radiation dose absorbed in soft tissue as a function of X-ray photon energy E for an incident photon fluence of 100 ph/μm^2. The black curves illustrate the X-ray transmission for soft tissue with thicknesses $d = 1$ mm and $d = 10$ mm. Attenuation coefficients μ are taken from the NIST database [37]. (B) Normalized SNR^2 behind the sample for a given dose in soft tissue with $d = 1$ mm and $d = 10$ mm. The green curves indicate the theoretical limit given by Poisson statistics (for details see Supplement 1). The orange and blue curves show the SNR^2 achievable by an indirect system with a 12 μm thick LSO scintillator or a Si (220) BM system, respectively, omitting further possible losses in the specific pixel-array detectors in use [34,38,39]. The asymmetry angle of the BM crystals was chosen for each energy to reach a resolution of 1.6 μm. Attenuation coefficients of LSO are taken from the NIST database [37]. (C) Normalized incoherent OTF of the magnifying optics of the indirect system and normalized coherent OTF of the Si (220) BM system at 30.5 keV with 1.6 μm resolution.

scintillator-based indirect detector systems have been used, which are constrained by a trade-off between X-ray detection efficiency and achievable resolution [26]. Alternatively, the X-ray image can be magnified with a so-called Bragg magnifier [27–33] and detected by an efficient large-area detector [34,35]. Although previous studies note the increased X-ray detection efficiency [30,32,36], the technique's potential for high dose efficiency remains unexplored. In particular, the superior detective quantum efficiency (DQE) at *high spatial frequencies*, which is decisive for dose-efficient high-resolution imaging, has not yet been considered and quantified experimentally in comparison to conventional systems.

This study reports on the development and application of a dose-efficient X-ray imaging system at micrometer spatial resolution operating close to the highest possible dose efficiency for PB-PCI. For this, we address the following aspects: (i) operating at X-ray energies with minimal dose for a given signal-to-noise ratio (SNR) and (ii) achieving high X-ray detection efficiency in this energy range by using a high-Z single-photon-counting detector (SPCD) combined with the above-mentioned X-ray magnifying crystal optics that (iii) exhibit uniform and nearly complete signal transfer for all spatial frequencies up to the targeted micrometer resolution. We confirm the increased imaging performance of the developed system by comparison to a conventional scintillator-based indirect detector system of similar resolution. We show an increased DQE by up to two orders of magnitude at high spatial frequencies for the targeted X-ray energies. The system thus extends the current methodological limits of micrometer resolution *in vivo* X-ray imaging, enabling a reduction of radiation load and prolongation of applicable exposure times. This opens up new possibilities for studies ranging from tracking internal morphology and morphodynamics to behavioral studies of organisms in hidden environments. As a pilot *in vivo* application, we investigate the behavior of tiny parasitoid wasps inside their host eggs, revealing the morphodynamics before and during emergence from the eggs over tens of minutes to hours.

2. RESULTS AND DISCUSSION

A. Considerations on Dose Efficiency

To begin with, we detail the above-mentioned aspects on how to minimize the dose required for a desired image quality. First, we consider the optimal X-ray photon energy E. The dose in the sample scales with the number of incident X-ray photons and their on average deposited energy. For soft tissue and a constant incident X-ray fluence, the deposited dose is shown in Fig. 1(A) as a function of E in the linear regime ($\mu d < 1$), where the dose is independent of the sample thickness d and with μ being the linear absorption coefficient. At low energies, the dose decreases rapidly with $\sim E^{-3}$ due to photoelectric absorption, levels off above 30 keV due to Compton scattering, and reaches a minimum at ~60 keV [40]. At this energy, one can in principle measure at the highest photon statistics for a given dose. However, the phase shift imposed on X-rays by the medium is proportional to E^{-1}, and thus the image contrast in PB-PCI also decreases with energy. Therefore, the SNR has to be optimized, given as the ratio of the phase-induced signal S and the noise N of the unscattered background field (zero-order beam). For different sample thicknesses d, we depict in Fig. 1(B) (green curves) the normalized SNR^2 behind the sample as a function of E at a constant dose deposited in the sample. The SNR^2 scales with the number of X-ray photons and hence is proportional to the dose. Since the signal in the SNR is sample-dependent, we normalized the curves to the theoretical maximum. For $d \leq 1$ mm, the maximal theoretically achievable SNR per dose is reached at 30 keV, being per se the optimal working energy, provided that the available flux of the X-ray source at this energy is sufficiently high. For thicker samples (dashed curve), the X-ray transmission decreases, in particular for low energies [see also black curves in Fig. 1(A)], thereby shifting the maximum to slightly higher energies. Note that for $\mu d > 1$ the local dose deposition is not homogeneous over the volume. Here, we compute the total dose in the sample, i.e., the average dose. Details on the calculations are given in Supplement 1.

Second, a high dose efficiency ideally also requires detection of every X-ray photon that passes through the sample. This, however, is technically challenging. For micrometer resolution X-ray imaging, the image needs to be magnified before being recorded

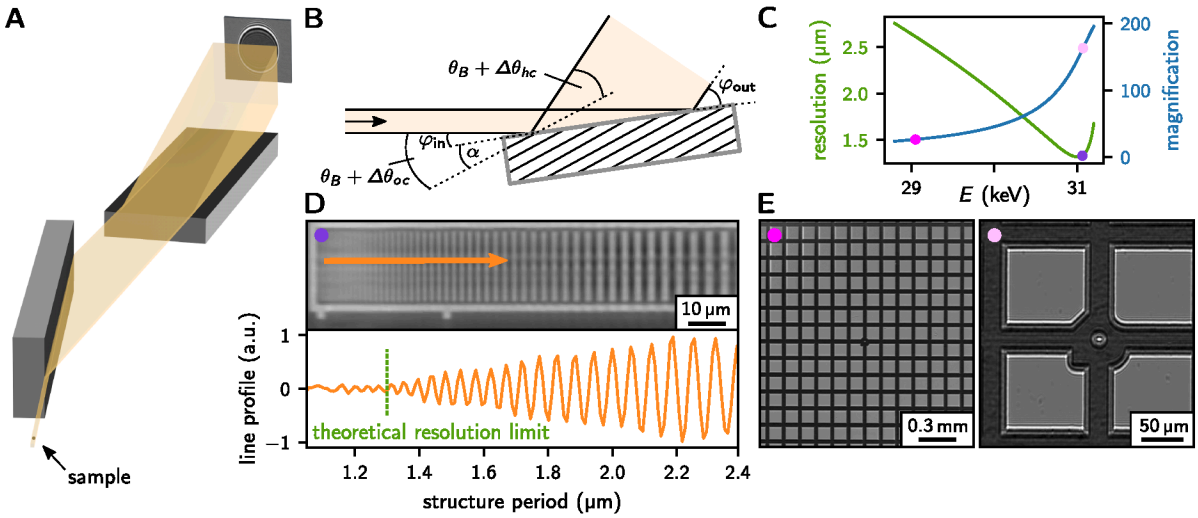

Fig. 2. Working principle of the Bragg magnifier system. (A) Schematics of the BM system. (B) Schematics of beam magnification by asymmetric Bragg diffraction [27] with the asymmetry angle α, the angles $\varphi_{in,out}$ between optical axis and crystal surface, the Bragg angle θ_B, and the corrections $\Delta\theta_{oc,hc}$ from dynamical diffraction theory [51]. (C) Theoretical intrinsic resolution and magnification of our Si (220) BM system with $\alpha = 5.92°$ as a function of the photon energy E [Eqs. (2) and (3)]. (D) Experimental verification of spatial resolution of 1.3 µm at 31 keV. The multidistance phase reconstruction [19,54] of a resolution line pattern reveals structure periods down to 1.3 m. In the line profile, we subtracted the background gradient for better visibility, which we attribute to source blur, especially at high spatial frequencies. (E) Radiograms of a gold grid show the adjustable magnification with photon energy (see also Visualization 1).

by a pixel-array camera. In commonly used scintillator-based indirect detector systems, a scintillator converts the X-ray photons into visible light, which is collected by an optical microscope and detected by the camera. The thickness of the scintillator is limited by the objective's depth of field, constrained by the desired spatial resolution [41]. This results in a reduced X-ray detection efficiency, i.e., the probability to detect an X-ray photon, which exacerbates with increasing photon energy and resolution. In contrast, direct magnification of the X-ray image allows exploitation of the high detection efficiency provided by large-pixel-array detectors. For the targeted working energy of 30 keV, an X-ray detection efficiency of almost 100% can be achieved by direct-converting SPCDs with a reasonably thick high-Z sensor, e.g., GaAs or CdTe connected to a Medipix3RX readout chip assembly with 55 µm pixel size [34,35]. The X-ray image can be magnified with a Bragg magnifier (BM) based on asymmetrically cut crystals [27–33]. Alternatively, magnification could be achieved by cone-beam geometry with focussing optics [42–47]. For a given dose, we compare the theoretically expected normalized SNR^2 obtained for a typical indirect system and a BM system at a resolution of 1.6 µm [Fig. 1(B)], omitting any further possible losses by electronic conversion and readout. For the BM system, the detection efficiency is inherently limited by the finite reflectivity of the crystals (>90% at $E \geq 25$ keV for Si 220 reflections). To achieve the targeted resolution with the indirect system, we chose a numerical aperture (NA) of 0.28 and a 12 µm thick LSO scintillator, which is to our knowledge one of the most suited thin-film scintillators for high-resolution X-ray imaging [26,41,48]. The absorption of the scintillator is an upper bound of the indirect system's X-ray detection efficiency. At the targeted energy of ~30 keV, the detection efficiency of the BM system is increased by at least a factor of 7.5 compared to the indirect system. Note that for dose-relevant imaging of a millimeter thick sample, the indirect system would ideally be operated at a lower energy of 11 keV, where the SNR^2 is 4.9-fold higher compared to 30 keV [Fig. 1(B)]. As the sample thickness increases, e.g., in local tomography [49], the transmission of the sample decreases and one is thus forced to increase the operating energy for the indirect system, in turn reducing its detection efficiency [dashed line in Fig. 1(B)].

Last, for the imaging performance it is even more crucial how the spatial frequencies of the object are transferred into the digital image. After maximizing the information content carried by the X-ray wavefield, the phase shift imprinted by the sample has to be converted into a measurable contrast. The image formation is best described in Fourier space by a cascade of transfer functions which state how strongly the spatial frequency components q in the wavefield are transferred through the imaging system. The total transfer function comprises the phase contrast transfer function (PCTF), the optical transfer function (OTF) of the magnifying optics, and the transfer function of the pixel-array detector. Here, we restrict the general considerations to the PCTF and the OTFs of the magnifying optics. For a discussion on the transfer functions of pixel-array detectors, which depend strongly on the particular device, we refer to the literature [34,38,39]. In general, the formation of an X-ray intensity image from a propagating wavefield is a nonlinear process. However, many biological samples can be considered as objects with a weak or weakly varying phase, which allows for a description by the PCTF [19]. The PCTF and thus the contrast in the measurable holograms are maximized by choosing the largest reasonable propagation distance z of the X-ray wavefield behind the sample, typically limited by source blur due to the extended X-ray source size [11]. Besides this propagation contrast formation, which both systems have in common, each system has its own additional OTF(q), quantifying how strongly the signal is diminished by the respective magnifying optics [50]. The coherent OTF of the BM system, relevant for PB-PCI of weak phase objects, is given by the square root of the crystals' reflectivity curves [51,52]. The OTF of the indirect system is given by the transfer function of the scintillator and the OTF of the microscope.

The former accounts for the spread of energy deposition generated by secondary particles; the latter is defined by the numerical aperture [26,41]. To keep it simple, we consider here only the incoherent OTF of the microscope as an upper bound, which is analytically accessible [41]. The OTF of the indirect system suppresses image information, in particular for high q containing the high-resolution components of the image [Fig. 1(C), orange curve]. In contrast, the normalized modulus of the BM's OTF is close to unity up to the resolution limit [Fig. 1(C), blue curve], ensuring almost ideal transfer of information.

Ultimately, for comparing the image quality of the two imaging systems experimentally, it is useful to consider the q-dependent $\mathrm{SNR}^2(q, D)$, which is also referred to as noise-equivalent quanta [53]. Since it is proportional to the dose D, the dose efficiency can be defined as $\mathrm{SNR}^2(q, D)/D$. For a comparison of the two imaging systems independent of the sample, we use the detective quantum efficiency $\mathrm{DQE}(q) = \mathrm{SNR}^2(q)/\mathrm{SNR}_0^2(q)$ as a figure of merit for the dose efficiency [53]. Ensuring the same input $\mathrm{SNR}_0^2(q)$, the gain in DQE is given by

$$G(q) = \frac{\mathrm{DQE}_{\mathrm{BM}}(q)}{\mathrm{DQE}_{\mathrm{ind}}(q)} = \frac{\mathrm{SNR}_{\mathrm{BM}}^2(q)}{\mathrm{SNR}_{\mathrm{ind}}^2(q)}. \tag{1}$$

At $q = 0$, we expect it to be at least the X-ray detection efficiency ratio, while it increases even further with q due to the higher OTF of the BM system. Last, we want to remind the reader that the indirect system should ideally be operated at the energy of its respective maximal dose efficiency, adjusted to the sample thickness [cf. Fig. 1(B)]. To compare the dose efficiency of both systems at different energies, the gain $G(q)$ has to be scaled with a corresponding factor deducible from Fig. 1(B). Summarizing, we expect the BM system to enhance significantly the q-dependent dose efficiency and accordingly the image quality compared to an indirect system.

B. Experimental Realization

In the following, we briefly outline the working principle of the BM [27–30], present our design considerations, and characterize the system experimentally. In general, a specific BM is designed for a small predefined energy window, within which the magnification can be varied by fine-tuning the energy. To reach highest dose efficiency, we design the BM system for an energy range of 29–31 keV using two Si single crystals with a nominal asymmetry angle $\alpha = 5.92°$ of the crystal surface normal with respect to the crystallographic [110] direction (for a detailed description of the setup, see Supplement 1). After monochromatization of the X-ray beam by a double-crystal monochromator, the BM crystals magnify the wavefield behind the sample in horizontal and vertical directions by asymmetric 220 Bragg reflection [Figs. 2(A) and 2(B)]. The magnification M originates from the strongly asymmetric diffraction geometry with α being close to the Bragg angle θ_B and is given by [28]

$$M = \frac{\sin\varphi_{\mathrm{out}}}{\sin\varphi_{\mathrm{in}}} = \frac{\sin(\theta_B + \Delta\theta_{hc} + \alpha)}{\sin(\theta_B + \Delta\theta_{oc} - \alpha)}, \tag{2}$$

where φ_{in} and φ_{out} are the incident and outgoing angles between the optical axis and the crystal surface, and $\Delta\theta_{oc}$ and $\Delta\theta_{hc}$ are correction terms of the incoming and outgoing beams, respectively, obtained from dynamical diffraction theory [51]. Since θ_B changes with energy, the magnification can be smoothly adjusted with E, in our case between $M = 20 - 180$ [Fig. 2(C)]. The tunability of the magnification is demonstrated experimentally by imaging a gold grid at various energies [Fig. 2(E) and Visualization 1]. As a side note, after magnification in a certain dimension, the further evolution of the interference pattern is negligible to good approximation [55]. Thus, the BM comes along with separate propagation distances z_x and z_y, given as the distance between the sample and the horizontally or vertically diffracting crystal, respectively [Fig. 2(A)]. This allows z_x and z_y to be individually set and optimized for the asymmetric source properties of third generation synchrotrons [56]. In the phase reconstruction, the different propagation distances have to be taken into account [55,57,58].

The smallest resolvable spatial wavelength λ_{min} is limited by the angular acceptance $2\delta_{oc}$ of the crystals. In accordance to Abbe's criterion, we have [29]

$$\lambda_{\mathrm{min}} = \frac{\lambda_0}{\sin\delta_{oc}}, \tag{3}$$

where λ_0 is the X-ray wavelength, and δ_{oc} is the Darwin width [51], which benefits from a large broadening by the strongly asymmetric diffraction geometry and can be tuned by the energy [Fig. 2(C)]. The theoretical resolution limit of our setup of 1.3 μm at 31 keV has been confirmed experimentally by imaging a test pattern with structure sizes down to 0.5 μm. A multidistance phase reconstruction [19,54] of the test pattern shows smallest resolvable structure periods corresponding to the expected resolution [Fig. 2(D)]. For more information on the reconstruction, see Supplement 1.

The X-ray reflectivity of a single crystal was measured to be $(96.5 \pm 0.6)\%$ at 30.5 keV, in close agreement with the theoretical value of 97.4%. The absorption of the 500 μm thick GaAs sensor of the SPCD in use can be estimated to be 97.6% [35,37]. The BM system comprising two crystals and the SPCD has therefore an overall X-ray detection efficiency of 91%.

For the indirect system (12 μm thick LSO scintillator, optical microscope with NA = 0.28, pco.edge 5.5 CMOS camera), the objective has a collection efficiency of the scintillation light of $0.5 \cdot (1 - \sqrt{1 - \mathrm{NA}^2/n^2}) = 0.6\%$ [59], where $n = 1.82$ is the refractive index of the scintillator. With the light yield of the scintillator being 40 photons/keV [60], we expect that on average 7.3 visible photons are collected by the objective per 30.5 keV X-ray photon absorbed in the scintillator. Including the quantum efficiency of the camera (>60%), the Poisson distribution of the optical photons will therefore only lead to a minor increase of the noise floor. Hence, the X-ray detection efficiency depends primarily on the X-ray absorption of the scintillator (12.3% at 30.5 keV). In contrast to an SPCD, being essentially free of readout noise, the CMOS camera adds a minor background noise. Further, incoherently scattered X-ray photons can degrade the image quality in the indirect system, while the incoherent background is filtered out by the BM's small energy acceptance. Overall, taking into account the measured reflectivity, we expect the X-ray detection efficiency of the BM system to be higher by more than a factor of 7.4 at 30.5 keV compared to the indirect system.

C. Comparison of Bragg Magnifier and Indirect System

We confirm experimentally the improved imaging performance of the BM system compared to the indirect system by measuring a Siemens star test pattern at multiple distances at the same energy of 30.5 keV [Figs. 3(A)–3(C)]. First, for a comparison of the image quality at the same nominal X-ray detection efficiency, we

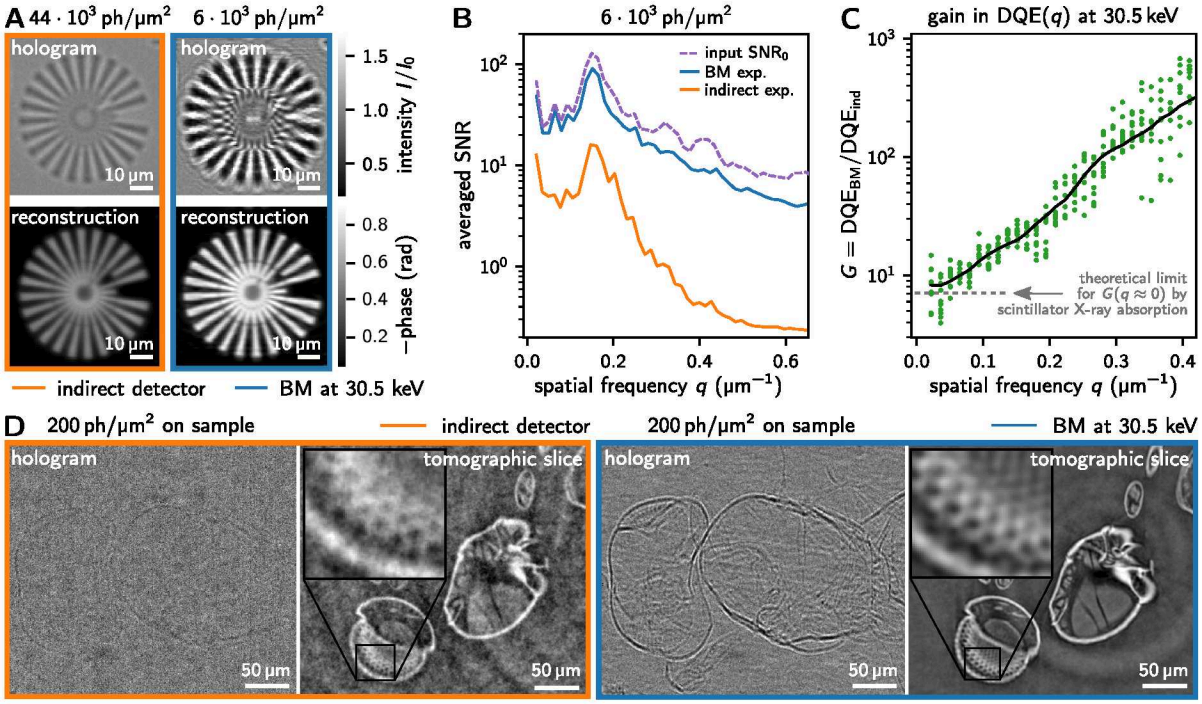

Fig. 3. Experimental comparison between a conventional indirect detector system and the Bragg magnifier at the same energy of 30.5 keV. (A) Flatfield-corrected holograms and multidistance phase reconstruction (10 distances) of a Siemens star test pattern. Note the increased X-ray intensity for the indirect system to compensate for the low X-ray absorption in the scintillator. (B) Measured SNR of the Siemens star holograms as a function of the spatial frequency q at the same incident X-ray fluence, averaged over 10 propagation distances and the azimuthal angle. For comparison, we simulate the input SNR_0 for perfect coherence. For details see Supplement 1. (C) Experimental gain $G(q)$ in DQE, extracted for each of the 10 propagation distances from the images used in (B); see Eq. (1) and Supplement 1. The solid line is a moving average and serves as a guide to the eye. (D) Flatfield-corrected holograms and single-distance tomographic reconstruction of a chalcid wasp (critical point dried *Lariophagus distinguendus*) acquired with both systems at comparably low incident X-ray fluence. For more information on the scan parameters see Supplement 1.

increased the flux for the indirect system by a factor ∼7 by removing absorption filters in order to compensate for its lower X-ray detection efficiency. Despite the lower dose in the BM images, the contrast and visibility of fine interference patterns in the holograms are still by far superior [Fig. 3(A), upper images]. This can be attributed to the BM system's higher OTF, especially at high spatial frequencies. The higher information content also translates to the multidistance phase reconstructed images [Fig. 3(A), lower images]. Prior to phase reconstruction, the indirect system images have been corrected by the incoherent OTF of the microscope [19] (see Supplement 1).

For a further quantitative analysis, we compare the q-dependent SNR of Siemens star holograms for the same incident X-ray intensity [Fig. 3(B)]. A detailed description of the evaluation is given in Supplement 1. Compared to the indirect system, the $\mathrm{SNR}(q)$ is significantly higher for the BM system. Further, the experimental data of the BM system are close to the simulation of the input field $\mathrm{SNR}_0(q)$. The simulation was performed without considering source blur, which explains the slight discrepancy with increasing q, besides minor influences by the SPCD in use [34,35]. The resulting gain in DQE at this energy, obtained from Eq. (1), is shown in Fig. 3(C). For the evaluation we take into account the different propagation distances. For $q \approx 0$, we observe the expected increase in DQE of $\gtrsim 7$ given by the absorption of the scintillator. For increasing q, $G(q)$ increases even further and reaches more than two orders of magnitude for $q > 0.3\ \mu\mathrm{m}^{-1}$. As a side note, we also tested a 50 µm thick LuAG scintillator, which performed even worse than the 12 µm thick LSO scintillator, especially at high q (see Supplement 1).

The impact of the BM system's higher detection efficiency on biological imaging is illustrated by imaging a chalcid wasp (*Lariophagus distinguendus*) with both systems at 30.5 keV and identical, comparably low photon fluence of 200 ph/µm² per frame [Fig. 3(D)]. For the indirect system, the specimen is hardly visible in the hologram, while the BM system shows good contrast. The superior imaging performance of the BM system becomes also apparent in the tomographic reconstruction, with insets enlarging the compound eye of the wasp, resolving finer structures.

Our measurements of the $\mathrm{SNR}(q)$ show that the indirect system behaves even less efficiently as we would surmise from considering the scintillator absorption and the OTF of the microscope. In addition, in the phase reconstruction for the indirect system the reconstructed phase shift is smaller than the expected value of −0.8 rad (1.4 µm gold structure), while for the BM system the reconstructed values agree to the expectation [Fig. 3(A)]. This can be explained by a spread of energy deposition in the scintillator, which increases with X-ray energy and further degrades the total transfer function of the indirect system [26,61]. Thus, to operate the indirect system at the optimal energy of ∼30 keV for highest possible dose efficiency, the scintillator must have not only high absorption but also low spread of energy deposition. As mentioned above, for our specific application with samples of size $d \lesssim 1$ mm the indirect system would best be operated at a lower energy of ∼11 keV. For this case, we estimate that the overall gain in dose efficiency of the BM system is a factor of about two at low spatial

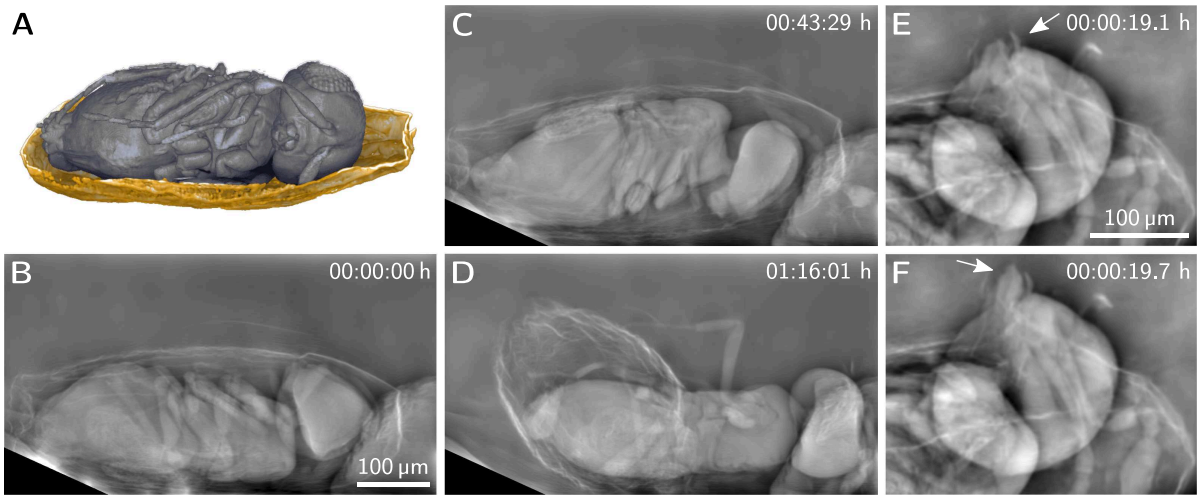

Fig. 4. *Trichogramma cacoeciae* wasps imaged *in vivo* with the BM system. (A) Volume rendering of tomographic data of a first *Trichogramma* individual inside its parasitized moth egg (*Sitotroga cerealella*). The egg shell (yellow) was sliced virtually to visualize the wasp (gray) inside the egg. (B)–(D) Phase reconstructed radiograms of a second individual emerging from its host egg (full series in Visualization 2). (E), (F) Flexible movement of mandibles, observed in a third individual (full series in Visualization 3). The arrows indicate that the wasp moves its mandibles independently from each other. For experimental details see Supplement 1.

frequencies and one order of magnitude at the desired resolution (see also Supplement 1). For thicker specimens or samples in a medium, higher energies are required for the indirect system, and the gain in dose efficiency of the BM system increases accordingly.

D. Pilot *in vivo* Study of Parasitoid Wasps within Their Hosts

As an *in vivo* pilot application, we exploit the high dose efficiency of the BM system to study the concealed behavior of parasitoid *Trichogramma* wasps related to the emergence from their host eggs over tens of minutes up to hours (see Fig. 4). *Trichogramma* wasps belong to the smallest known insects. By parasitizing the eggs of a wide range of crop-infesting butterfly and moth species, they are the most widely used biological control agent [62] and therefore possess enormous economic value [63–65]. Despite being among the best-studied parasitic insects [66], their concealed behavior within their hosts is largely unknown. The BM system allowed us to record long *in vivo* cine-radiographic data of several individuals, revealing morphodynamics before and during emergence from the eggs. Figure 4(A) shows a volume rendering of a tomographic dataset of a first specimen shortly before emergence. For a second individual, Figs. 4(B)–4(D) display phase reconstructed radiograms of the wasp during emergence at different moments in time. The full cine-radiographic dataset is given in Visualization 2. Images were denoised by a neural network, trained with the Noise2Noise method [67]. Details of the method application can be found in [68]. The wasp was filmed in several sequences, intermitted by radiation-free pauses, over a total duration of 1.25 h and a total X-ray exposure of 30 min. After emergence, we did not observe any abnormalities in the wasp's behavior. The estimated dose is ∼7 mGy per frame, yielding an overall dose of ∼200 Gy, which agrees to dose levels reported in literature to have no observable physiological effects on small animals [10]. We identified characteristic movement patterns and behavioral acts of the wasp, which are described in detail in Supplement 1. In the dataset of another individual, the movement of the mandibles during the biting process became particularly well visible; see Figs. 4(E), 4(F), and Visualization 3 (dose per frame of ∼70 mGy and total dose of ∼90 Gy using a higher flux and Ge crystals; see Supplement 1). As opposed to the larger *L. distinguendus*, which has been shown to employ its mandibles in a chisel-like manner to bite through a stiff wheat grain [69], *Trichogramma cacoeciae* is here observed to use its mandibles independently from each other to penetrate the more pliable egg shell. This versatility demonstrates how flexible mandibular movement allowed chalcid wasps to exploit a variety of hosts, most likely being a key factor for their evolutionary success and their enormous diversification [69].

3. CONCLUSION

We present a considerable increase in dose efficiency in micrometer-resolution X-ray imaging of soft tissues by combining highly coherent synchrotron radiation, a high-Z single-photon-counting detector, and Bragg magnifier crystal optics, and by operating at X-ray energies ∼30 keV that allow a minimum dose for a desired signal-to-noise ratio. We show that the developed BM system works close to the highest possible dose efficiency for propagation-based phase contrast imaging, owing not only to its X-ray detection efficiency of over 90% but also its advantageous optical transfer function. Compared to a scintillator-based detector system at these energies, we measure an increase in DQE of more than two orders of magnitude for high spatial frequencies, which are crucial for high spatial resolution. For applications where the efficiency of indirect systems can be improved by working at lower energy, we still estimate a gain in dose efficiency of the BM system of one order of magnitude at high spatial frequencies, which contain the relevant high-resolution components of the image. Even though indirect detectors benefit from continuously ongoing developments of scintillators [70], optics [71], and cameras [72], the BM system intrinsically outperforms any lens-based optically magnifying system by its constantly high OTF for all spatial frequencies up to its resolution limit. The BM system enables a substantial increase of observation times in *in vivo* studies at micrometer resolution, allowing us to film the concealed behavior of parasitoid *Trichogramma* wasps for more than 30 min. This pilot

study provides a detailed analysis of their movement patterns and behavioral acts before and during emergence from their host eggs and demonstrates the flexible biting functionality of their mandibles. We believe that due to its high dose efficiency, BM-based X-ray imaging will find broad application, not only for *in vivo* imaging in life sciences but also for *in situ* studies of dose-sensitive materials and processes.

Funding. Bundesministerium für Bildung und Forschung (05K2016, 05K2019).

Acknowledgment. We acknowledge DESY (Hamburg, Germany), a member of the Helmholtz Association HGF, for the provision of experimental facilities. Parts of this research were carried out at P23, PETRA III, in the frame of the KIT-DESY "Hierarchical Imaging Karlsruhe" collaboration, and we would like to thank Azad Khadiev and Atula Poduval for technical support. We acknowledge the KIT Light Source for the allocation of preparational beamtime; the Institute for Beam Physics and Technology (IBPT) for the operation of the storage ring, the Karlsruhe Reseach Accelerator (KARA); KIT technical staff for outstanding support, in particular Stefan Uhlemann, David Haas, Tobias Hilverling, and Julian Schäfer; the DESY transport group and DESY hall operator for assistance during transportation of the equipment; Rolf Simon for support during beamtime preparations; Daniel Hänschke, Ralf Hofmann, and Patrik Vagovic for fruitful discussions; and Stephen Doyle for language revision.

Disclosures. The authors declare no conflicts of interest.

Data availability. Data underlying the results presented in this paper are available in Supplement 1, in Dataset 1, Ref. [73], and Dataset 2, Ref. [74]. See Code 1, Ref. [75] for the source code used to generate Fig. S4 in Supplement 1.

Supplemental document. See Supplement 1 for supporting content.

REFERENCES

1. O. Betz, U. Wegst, D. Weide, M. Heethoff, L. Helfen, W.-K. Lee, and P. Cloetens, "Imaging applications of synchrotron X-ray phase-contrast microtomography in biological morphology and biomaterials science. I. General aspects of the technique and its advantages in the analysis of millimetre-sized arthropod structure," J. Microsc. **227**, 51–71 (2007).
2. T. van de Kamp, P. Vagovič, T. Baumbach, and A. Riedel, "A biological screw in a beetle's leg," Science **333**, 52 (2011).
3. M. E. Dickinson, A. M. Flenniken, X. Ji, *et al.*, "High-throughput discovery of novel developmental phenotypes," Nature **537**, 508–514 (2016).
4. A. Cau, V. Beyrand, D. F. Voeten, V. Fernandez, P. Tafforeau, K. Stein, R. Barsbold, K. Tsogtbaatar, P. J. Currie, and P. Godefroit, "Synchrotron scanning reveals amphibious ecomorphology in a new clade of bird-like dinosaurs," Nature **552**, 395–399 (2017).
5. M. Töpperwien, F. van der Meer, C. Stadelmann, and T. Salditt, "Three-dimensional virtual histology of human cerebellum by X-ray phase-contrast tomography," Proc. Natl. Acad. Sci. USA **115**, 6940–6945 (2018).
6. T. van de Kamp, A. H. Schwermann, T. dos Santos Rolo, P. D. Lösel, T. Engler, W. Etter, T. Faragó, J. Göttlicher, V. Heuveline, A. Kopmann, B. Mähler, T. Mörs, J. Odar, J. Rust, N. Tan Jerome, M. Vogelgesang, T. Baumbach, and L. Krogmann, "Parasitoid biology preserved in mineralized fossils," Nat. Commun. **9**, 3325 (2018).
7. Y. Ding, D. J. Vanselow, M. A. Yakovlev, S. R. Katz, A. Y. Lin, D. P. Clark, P. Vargas, X. Xin, J. E. Copper, V. A. Canfield, K. C. Ang, Y. Wang, X. Xiao, F. D. Carlo, D. B. van Rossum, P. L. Riviere, and K. C. Cheng, "Computational 3D histological phenotyping of whole zebrafish by X-ray histotomography," eLife **8**, e44898 (2019).
8. K. Trinajstic, J. A. Long, S. Sanchez, C. A. Boisvert, D. Snitting, P. Tafforeau, V. Dupret, A. M. Clement, P. D. Currie, B. Roelofs, J. J. Bevitt, M. S. Y. Lee, and P. E. Ahlberg, "Exceptional preservation of organs in Devonian placoderms from the Gogo lagerstätte," Science **377**, 1311–1314 (2022).
9. M. W. Westneat, O. Betz, R. W. Blob, K. Fezzaa, W. J. Cooper, and W.-K. Lee, "Tracheal respiration in insects visualized with synchrotron X-ray imaging," Science **299**, 558–560 (2003).
10. J. J. Socha, M. W. Westneat, J. F. Harrison, J. S. Waters, and W.-K. Lee, "Real-time phase-contrast X-ray imaging: a new technique for the study of animal form and function," BMC Biol. **5**, 1–15 (2007).
11. J. Moosmann, A. Ershov, V. Altapova, T. Baumbach, M. S. Prasad, C. LaBonne, X. Xiao, J. Kashef, and R. Hofmann, "X-ray phase-contrast *in vivo* microtomography probes new aspects of *Xenopus* gastrulation," Nature **497**, 374–377 (2013).
12. S. M. Walker, D. A. Schwyn, R. Mokso, M. Wicklein, T. Müller, M. Doube, M. Stampanoni, H. G. Krapp, and G. K. Taylor, "*In vivo* time-resolved microtomography reveals the mechanics of the blowfly flight motor," PLoS Biol. **12**, e1001823 (2014).
13. T. dos Santos Rolo, A. Ershov, T. van de Kamp, and T. Baumbach, "In vivo X-ray cine-tomography for tracking morphological dynamics," Proc. Natl. Acad. Sci. USA **111**, 3921–3926 (2014).
14. C. Schmitt, A. Rack, and O. Betz, "Analyses of the mouthpart kinematics in *Periplaneta americana* (Blattodea, Blattidae) using synchrotron-based X-ray cineradiography," J. Exp. Biol. **217**, 3095–3107 (2014).
15. R. Mokso, D. A. Schwyn, S. M. Walker, M. Doube, M. Wicklein, T. Müller, M. Stampanoni, G. K. Taylor, and H. G. Krapp, "Four-dimensional *in vivo* X-ray microscopy with projection-guided gating," Sci. Rep. **5**, 8727 (2015).
16. O. Bolmin, J. J. Socha, M. Alleyne, A. C. Dunn, K. Fezzaa, and A. A. Wissa, "Nonlinear elasticity and damping govern ultrafast dynamics in click beetles," Proc. Natl. Acad. Sci. USA **118**, e2014569118 (2021).
17. A. Momose and J. Fukuda, "Phase-contrast radiographs of nonstained rat cerebellar specimen," Med. Phys. **22**, 375–379 (1995).
18. S. Wilkins, T. E. Gureyev, D. Gao, A. Pogany, and A. Stevenson, "Phase-contrast imaging using polychromatic hard X-rays," Nature **384**, 335–338 (1996).
19. P. Cloetens, W. Ludwig, J. Baruchel, D. Van Dyck, J. Van Landuyt, J. Guigay, and M. Schlenker, "Holotomography: Quantitative phase tomography with micrometer resolution using hard synchrotron radiation x rays," Appl. Phys. Lett. **75**, 2912–2914 (1999).
20. D. Paganin, S. C. Mayo, T. E. Gureyev, P. R. Miller, and S. W. Wilkins, "Simultaneous phase and amplitude extraction from a single defocused image of a homogeneous object," J. Microsc. **206**, 33–40 (2002).
21. T. Weitkamp, A. Diaz, C. David, F. Pfeiffer, M. Stampanoni, P. Cloetens, and E. Ziegler, "X-ray phase imaging with a grating interferometer," Opt. Express **13**, 6296–6304 (2005).
22. A. Momose, W. Yashiro, Y. Takeda, Y. Suzuki, and T. Hattori, "Phase tomography by X-ray talbot interferometry for biological imaging," Jpn. J. Appl. Phys. **45**, 5254 (2006).
23. P. C. Diemoz, P. Coan, C. Glaser, and A. Bravin, "Absorption, refraction and scattering in analyzer-based imaging: comparison of different algorithms," Opt. Express **18**, 3494–3509 (2010).
24. M. Viermetz, L. Birnbacher, M. Willner, K. Achterhold, F. Pfeiffer, and J. Herzen, "High resolution laboratory grating-based X-ray phase-contrast CT," Sci. Rep. **8**, 15884 (2018).
25. S. Huhn, L. M. Lohse, J. Lucht, and T. Salditt, "Fast algorithms for nonlinear and constrained phase retrieval in near-field X-ray holography based on Tikhonov regularization," Opt. Express **30**, 32871–32886 (2022).
26. L. Wollesen, F. Riva, P.-A. Douissard, K. Pauwels, T. Martin, and C. Dujardin, "Scintillating thin film design for ultimate high resolution X-ray imaging," J. Mater. Chem. C **10**, 9257–9265 (2022).
27. W. J. Boettinger, H. E. Burdette, and M. Kuriyama, "X-ray magnifier," Rev. Sci. Instrum. **50**, 26–30 (1979).
28. K. Kobayashi, K. Izumi, H. Kimura, S. Kimura, T. Ibuki, Y. Yokoyama, Y. Tsusaka, Y. Kagoshima, and J. Matsui, "X-ray phase-contrast imaging with submicron resolution by using extremely asymmetric Bragg diffractions," Appl. Phys. Lett. **78**, 132–134 (2001).
29. R. D. Spal, "Submicrometer resolution hard X-ray holography with the asymmetric Bragg diffraction microscope," Phys. Rev. Lett. **86**, 3044 (2001).
30. M. Stampanoni, G. Borchert, R. Abela, and P. Rüegsegger, "Bragg magnifier: a detector for submicrometer x-ray computer tomography," J. Appl. Phys. **92**, 7630–7635 (2002).
31. P. Modregger, D. Lübbert, P. Schäfer, and R. Köhler, "Magnified X-ray phase imaging using asymmetric Bragg reflection: experiment and theory," Phys. Rev. B **74**, 054107 (2006).
32. P. Vagovič, D. Korytar, A. Cecilia, E. Hamann, L. Švéda, D. Pelliccia, J. Härtwig, Z. Zápražný, P. Oberta, I. Dolbnya, K. Shawney, U. Fleschig, M. Fiederle, and T. Baumbach, "High-resolution high-efficiency X-ray imaging system based on the in-line Bragg magnifier and the Medipix detector," J. Synchrotron Radiat. **20**, 153–159 (2013).
33. K. Hirano, Y. Yamashita, Y. Takahashi, and H. Sugiyama, "Development of variable-magnification X-ray Bragg optics," J. Synchrotron Radiat. **22**, 956–960 (2015).

34. E. Hamann, T. Koenig, M. Zuber, A. Cecilia, A. Tyazhev, O. Tolbanov, S. Procz, A. Fauler, T. Baumbach, and M. Fiederle, "Performance of a Medipix3RX spectroscopic pixel detector with a high resistivity gallium arsenide sensor," IEEE Trans. Med. Imaging **34**, 707–715 (2014).
35. D. Pennicard, S. Smoljanin, B. Struth, H. Hirsemann, A. Fauler, M. Fiederle, O. Tolbanov, A. Zarubin, A. Tyazhev, G. Shelkov, and H. Graafsma, "The LAMBDA photon-counting pixel detector and high-Z sensor development," J. Instrum. **9**, C12026 (2014).
36. M. Stampanoni, G. Borchert, and R. Abela, "Towards nanotomography with asymmetrically cut crystals," Nucl. Instrum. Methods Phys. Res. A **551**, 119–124 (2005).
37. J. H. Hubbell and S. M. Seltzer, "Tables of X-ray mass attenuation coefficients and mass energy-absorption coefficients 1 keV to 20 MeV for elements Z = 1 to 92 and 48 additional substances of dosimetric interest," Ionizing Radiation Division, National Institute of Standards and Technology-PL (1995).
38. A. Mittone, I. Manakov, L. Broche, C. Jarnias, P. Coan, and A. Bravin, "Characterization of a sCMOS-based high-resolution imaging system," J. Synchrotron Radiat. **24**, 1226–1236 (2017).
39. J. Scholz, L. Birnbacher, C. Petrich, M. Riedel, L. Heck, S. Gkoumas, T. Sellerer, K. Achterhold, and J. Herzen, "Biomedical X-ray imaging with a GaAs photon-counting detector: A comparative study," APL Photonics **5**, 106108 (2020).
40. J. Bille and W. Schlegel, *Medizinische Physik 2* (Springer, 2002).
41. J. W. Goodman, *Introduction to Fourier Optics* (Roberts and Company, 2005).
42. P. Kirkpatrick and A. V. Baez, "Formation of optical images by X-rays," J. Opt. Soc. Am. **38**, 766–774 (1948).
43. G. Schmahl, D. Rudolph, B. Niemann, and O. Christ, "Zone-plate X-ray microscopy," Q. Rev. Biophys. **13**, 297–315 (1980).
44. A. Snigirev, V. Kohn, I. Snigireva, and B. Lengeler, "A compound refractive lens for focusing high-energy X-rays," Nature **384**, 49–51 (1996).
45. F. Pfeiffer, C. David, M. Burghammer, C. Riekel, and T. Salditt, "Two-dimensional X-ray waveguides and point sources," Science **297**, 230–234 (2002).
46. H. Kang, J. Maser, G. Stephenson, C. Liu, R. Conley, A. Macrander, and S. Vogt, "Nanometer linear focusing of hard x rays by a multilayer Laue lens," Phys. Rev. Lett. **96**, 127401 (2006).
47. S. Flenner, J. Hagemann, F. Wittwer, E. Longo, A. Kubec, A. Rothkirch, C. David, M. Müller, and I. Greving, "Hard X-ray full-field nanoimaging using a direct photon-counting detector," J. Synchrotron Radiat. **30**, 390–399 (2023).
48. T. Martin and A. Koch, "Recent developments in X-ray imaging with micrometer spatial resolution," J. Synchrotron Radiat. **13**, 180–194 (2006).
49. G. Lovric, R. Mokso, F. Arcadu, I. Vogiatzis Oikonomidis, J. C. Schittny, M. Roth-Kleiner, and M. Stampanoni, "Tomographic in vivo microscopy for the study of lung physiology at the alveolar level," Sci. Rep. **7**, 1–10 (2017).
50. J. M. Blackledge, *Digital Image Processing: Mathematical and Computational Methods* (Elsevier, 2005).
51. A. Authier, *Dynamical Theory of X-ray Diffraction* (Oxford University, 2004), Vol. **11**.
52. T. Davis, "X-ray diffraction imaging using perfect crystals," J. X-Ray Sci. Technol. **6**, 317–342 (1996).
53. I. A. Cunningham and R. Shaw, "Signal-to-noise optimization of medical imaging systems," J. Opt. Soc. Am. A **16**, 621–632 (1999).
54. L. M. Lohse, A.-L. Robisch, M. Töpperwien, S. Maretzke, M. Krenkel, J. Hagemann, and T. Salditt, "A phase-retrieval toolbox for X-ray holography and tomography," J. Synchrotron Radiat. **27**, 852–859 (2020).
55. P. Modregger, D. Lübbert, P. Schäfer, R. Köhler, T. Weitkamp, M. Hanke, and T. Baumbach, "Fresnel diffraction in the case of an inclined image plane," Opt. Express **16**, 5141–5149 (2008).
56. D. H. Bilderback, P. Elleaume, and E. Weckert, "Review of third and next generation synchrotron light sources," J. Phys. B **38**, S773 (2005).
57. P. Vagovič, L. Švéda, A. Cecilia, E. Hamann, D. Pelliccia, E. Gimenez, D. Korytár, K. M. Pavlov, Z. Zápražný, M. Zuber, T. Koenig, M. Olbinado, W. Yashiro, A. Momose, M. Fiederle, and T. Baumbach, "X-ray Bragg magnifier microscope as a linear shift invariant imaging system: image formation and phase retrieval," Opt. Express **22**, 21508–21520 (2014).
58. S. Hrivňak, J. Uličný, and P. Vagovič, "Fast Fresnel propagation through a set of inclined reflecting planes applicable for X-ray imaging," Opt. Express **26**, 34569–34579 (2018).
59. M. Müller, *Introduction to Confocal Fluorescence Microscopy* (SPIE, 2006), Vol. **69** Appendix B.
60. P.-A. Douissard, A. Cecilia, T. Martin, V. Chevalier, M. Couchaud, T. Baumbach, K. Dupré, M. Kühbacher, and A. Rack, "A novel epitaxially grown LSO-based thin-film scintillator for micro-imaging using hard synchrotron radiation," J. Synchrotron Radiat. **17**, 571–583 (2010).
61. ESRF, "Modelling of the MTF performance of high spatial resolution X-ray detectors," (2016). [Online; accessed 18 May 2023].
62. L.-Y. Li, "Worldwide use of Trichogramma for biological control on different crops: a survey," in *Biological Control with Egg Parasitoids* (1994).
63. Z.-Y. Wang, K.-L. He, F. Zhang, X. Lu, and D. Babendreier, "Mass rearing and release of Trichogramma for biological control of insect pests of corn in China," Biol. Control **68**, 136–144 (2014).
64. L.-S. Zang, S. Wang, F. Zhang, and N. Desneux, "Biological control with Trichogramma in China: history, present status and perspectives," Annu. Rev. Entomol **66**, 463–484 (2021).
65. A. Cherif, R. Mansour, and K. Grissa-Lebdi, "The egg parasitoids Trichogramma: from laboratory mass rearing to biological control of lepidopteran pests," Biocontrol Sci. Technol. **31**, 661–693 (2021).
66. A. Ivezić, B. Trudić, and G. Draškić, "The usage of beneficial insects as a biological control measure in large-scale farming-a case study review on Trichogramma spp," Acta agriculturae Slovenica **118**, 1–13 (2022).
67. J. Lehtinen, J. Munkberg, J. Hasselgren, S. Laine, T. Karras, M. Aittala, and T. Aila, "Noise2Noise: Learning image restoration without clean data," arXiv, arXiv:1803.04189 (2018).
68. Y. Zharov, E. Ametova, R. Spiecker, T. Baumbach, G. Burca, and V. Heuveline, "Shot noise reduction in radiographic and tomographic multi-channel imaging with self-supervised deep learning," Opt. Express **31**, 26226–26244 (2023).
69. T. van de Kamp, I. Mikó, A. H. Staniczek, B. Eggs, D. Bajerlein, T. Faragó, L. Hagelstein, E. Hamann, R. Spiecker, T. Baumbach, P. Janšta, and L. Krogmann, "Evolution of flexible biting in hyperdiverse parasitoid wasps," Proc. R. Soc. B **289**, 20212086 (2022).
70. Z. Zhang, H. Dierks, N. Lamers, C. Sun, K. Nováková, C. Hetherington, I. G. Scheblykin, and J. Wallentin, "Single-crystalline perovskite nanowire arrays for stable X-ray scintillators with micrometer spatial resolution," ACS Appl. Nano Mater. **5**, 881–889 (2021).
71. M. Bührer, M. Stampanoni, X. Rochet, F. Büchi, J. Eller, and F. Marone, "High-numerical-aperture macroscope optics for time-resolved experiments," J. Synchrotron Radiat. **26**, 1161–1172 (2019).
72. Z. Wang, K. Anagnost, C. W. Barnes, D. M. Dattelbaum, E. R. Fossum, E. Lee, J. Liu, J. J. Ma, W. Z. Meijer, W. Nie, C. M. Sweeney, A. C. Therrien, H. Tsai, and X. Yue, "Billion-pixel X-ray camera (BiPC-X)," Rev. Sci. Instrum. **92**, 043708 (2021).
73. R. Spiecker, P. Pfeiffer, A. Biswal, *et al.*, "Raw and processed data for comparison between a scintillator-based indirect detector system and a Bragg magnifier system," figshare (2023), https://doi.org/10.6084/m9.figshare.23703729.
74. R. Spiecker, P. Pfeiffer, A. Biswal, *et al.*, "Data of Movie S2 and S3," figshare (2023), https://doi.org/10.6084/m9.figshare.23703681.
75. R. Spiecker and M. Spiecker, "Source code to reproduce Fig. S4," figshare (2023), https://doi.org/10.6084/m9.figshare.24295120.